Roll-to-Roll Printing of Perovskite Solar Cells

Benjia Dou,[†,‡] James B. Whitaker,[†] Karsten Bruening,[§] David T. Moore,[†] Lance M. Wheeler,[†] John Ryter,[†] Nicholas J. Breslin,[†] Joseph J. Berry,[†] Sean M. Garner,[∥] Frank S. Barnes,[‡] Sean E. Shaheen,[‡,⊥] Christopher J. Tassone,[§] Kai Zhu,[†] and Maikel F. A. M. van Hest*[,†]

[†]National Renewable Energy Laboratory, Golden, Colorado 80401, United States

[‡]Department of Electrical, Computer and Energy Engineering, University of Colorado Boulder, Boulder, Colorado 80302, United States

[§]Stanford Synchrotron Radiation Lightsource, SLAC National Accelerator Laboratory, Menlo Park, California 94025, United States

[∥]Corning Research & Development Corporation, Corning, New York 14830, United States

[⊥]Renewable and Sustainable Energy Institute, University of Colorado Boulder, Boulder, Colorado 80309 United States

ABSTRACT: High efficiency combined with transformative roll-to-roll (R2R) printability makes metal halide perovskite-based solar cells the most promising solar technology to address the terawatt challenge of the future energy demand. However, translation from lab-scale deposition solution processing techniques to large-scale R2R methods has typically led to reduced photovoltaic performance. Here, we demonstrate large-scale, highly crystalline, uniaxially oriented, smooth perovskite films printed at room temperature and in the ambient environment. Confirmed with high speed in situ X-ray diffraction measurements, the perovskite films reach 98% of relative crystallinity at room temperature and display high texture within 1 s of the coating. We demonstrate an all-blade-coated metal halide perovskite cell with power conversion efficiency (PCE) up to 19.6%, a slot-die coated cell with a PCE of 17.3%, and a partially R2R slot-die coated flexible glass-based cell efficiency of 14.1%. The developed printing method can be applied to diverse perovskite compositions, enabling a variety of bandgaps to pave the way for the future R2R printing of highly efficient perovskite−perovskite tandem cells.

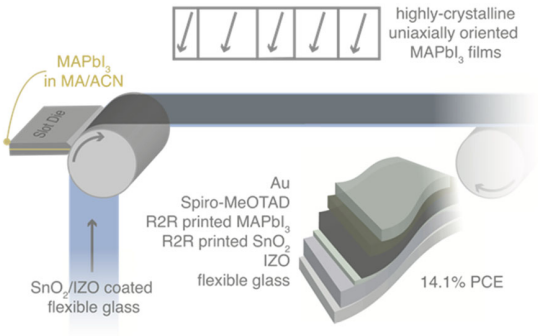

Compared to traditional vacuum-processed photovoltaic (PV) technologies (Silicon, GaAs), solution-processable thin film PV technologies (organic, quantum dot, perovskite) offer an unprecedented opportunity for manufacturing solar cells with high throughput using roll-to-roll (R2R) printing, a technology used to print the hundreds of millions of newspaper copies worldwide each day.[1] Among these thin film PV technologies, metal halide perovskites (MHPs) have generated monumental interest with their promise to truly revolutionize the current energy generation landscape due to its excellent efficiency,[2] abundant raw material,[3] and, most importantly, high defect tolerance[4] that is vital in the R2R printing process.[5] The MHP PV field, after less than a decade of intense research, has reached a technological maturity where scalable processing is needed to facilitate commercialization of the technology.[6]

The majority of the device efficiency improvements in the MHP field have been centered around the solution chemistry and morphological control that is optimized for spin-coating, which is, unfortunately, mostly not R2R-compatible. On the other hand, there are some recent breakthroughs to successfully deposit perovskite films with meniscus-guided coating techniques, such as blade and slot-die coating, which are either transferable or directly compatible with R2R coating systems. With extensive investigations on the solution chemistry and processing parameters, multiple >19% PCE blade-coated devices are reported by solvent exchange[7] or at elevated temperature.[8−11] These impressive results highlight the importance of accelerated crystallization in meniscus-guided coating of MHP, but little attention has been paid to the control of crystal growth orientation in such processing and the applicability of developed processing to R2R printing.

In this work, a room-temperature perovskite printing method is presented. Using a solution chemistry that allows very fast (∼1s) crystallization, the printing method allows for fabrication of uniaxially oriented, less horizonal grain boundaries, very smooth perovskite films that yield up to

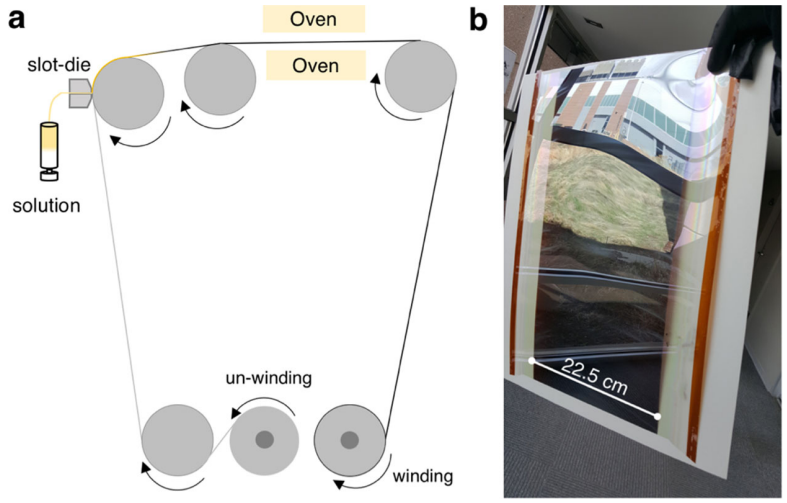

Figure 1. R2R slot-die coating setup (a) and resulting perovskite film (b).

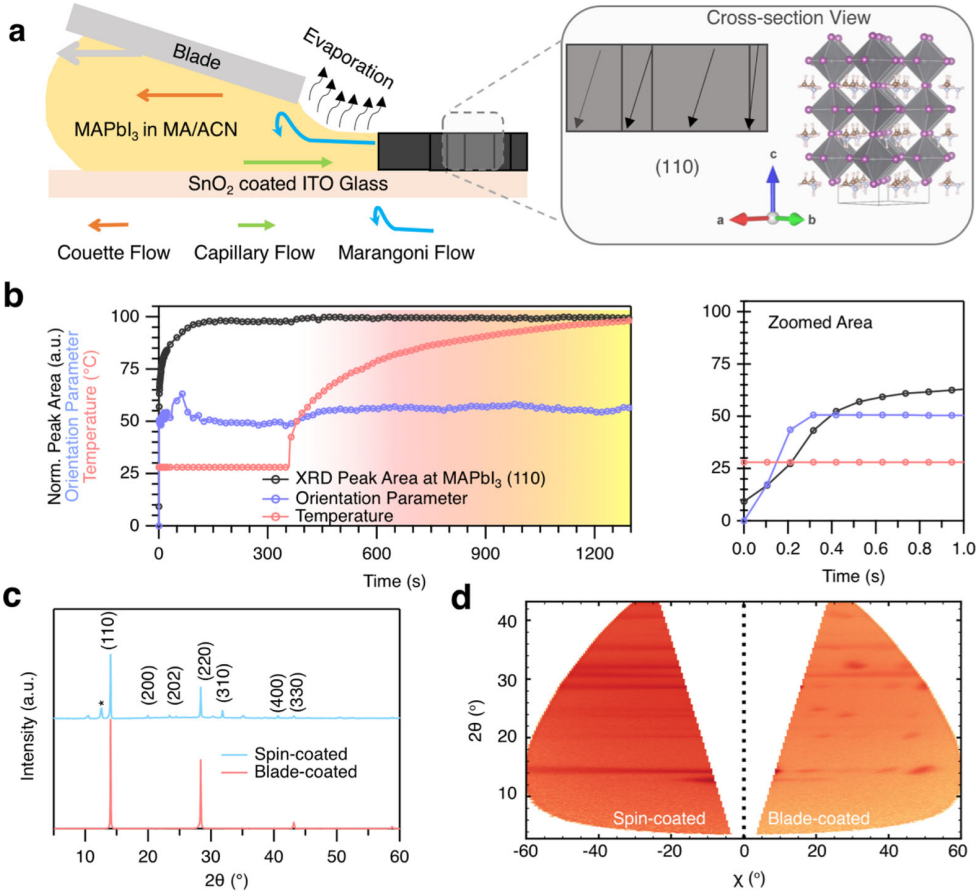

Figure 2. (a) Schematic representation of blade coating. (b) Temperature profile (orange lines), integrated XRD peak area (black lines), and Maier–Saupe orientation distribution parameter (pink lines) tracked from blade coating/high-speed (50 ms intervals) in situ XRD measurement over 20 min (left) and zoomed area of the initial 1 s (right). (c) XRD pattern of spin-coated (blue line) and blade-coated (orange line) films. (d) 2D-XRD of spin-coated (left) and blade-coated (right) films.

19.6% PCE in an all-blade-coated structure (excluding the top and bottom contact layers). The blade-coated prototype is extended to slot-die coating on rigid glass substrates to obtain a PCE of 17.3% and then to a R2R coating system (Figure 1) with 20 m long flexible glass as the substrate to yield a PCE of 14.1%. The R2R method is not limited to the prototype MHP material, methylammonium lead iodide ($MAPbI_3$), and can easily be applied to other perovskite material systems. Most notably, we demonstrate a bromide-containing high-bandgap (1.71 eV) perovskite that will enable all-R2R-printed, low-cost, high-efficiency perovskite–perovskite tandem devices.

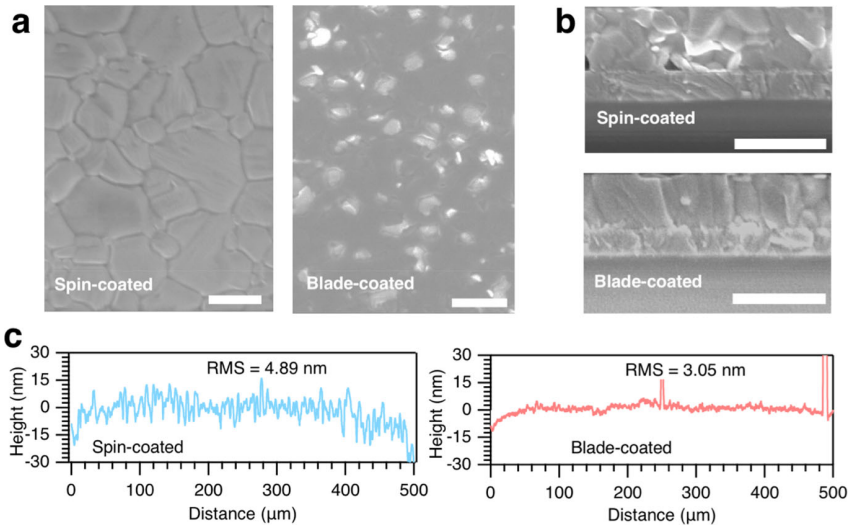

Figure 3. (a) Top-view SEM images of spin-coated (left) and blade-coated (right) films. The scale bar is 500 nm. (b) Cross-sectional SEM images of spin-coated (top) and blade-coated (bottom) films. The scale bar is 500 nm. (c) Surface roughness profiling of films from spin-coating (left) and blade-coating (right).

Meniscus-Guided Coating of a Highly Concentrated Solution. It has been suggested that the ideal MHP absorber should minimize the nonradiative losses and thus be defect-free with high crystallinity, benign grain boundaries, and ideal surface morphology (i.e., smooth compact pinhole-free surface).[12] The crystallization process or the precursor-to-film conversion can be described by the LaMer curve, presented in Figure S1, where four stages from solution to thin film are identified: prenucleation (stage I); nucleation (stage II); nucleation and crystal growth (stage III); and crystal growth (stage IV). Fast crystallization of MHP is typically obtained by introducing rapid concentration changes when the nucleation from the precursor film starts, at stage III, through external forces such as solvent exchange,[13] vacuum,[14] flash annealing,[3,15] elevated temperature,[10] gas flow,[16] or a mixture thereof. To implement the desired fast crystallization while maintaining ideal MHP absorber properties in R2R printing (Figure 1) without using any of the above external forces, we propose the following strategies: (1) start with a highly concentrated solution (>1M); (2) apply a low boiling point solvent so that the concentration change from the highly concentrated solution to supersaturated solution can be fast. With a boiling point of ~78 °C, methylamine-charged (10% w/w) acetonitrile (MA/ACN)[17] is chosen to be the solvent, and a highly concentrated $MAPbI_3$ solution is prepared (see Figures S2–S4). To note, ACN is a low boiling point (82 °C) polar aprotic solvent, but it does not dissolve some perovskite precursor salts such as PbI_2. Using blade coating as the prototype for R2R coating, the as-prepared solution is coated on SnO_2/ITO/glass substrates. Due to fast solvent evaporation, as illustrated in Figure 2a, the capillary flow toward the contact line and Marangoni flow at the front of the meniscus are enhanced along with the Couette flow induced by the blade shear force.[18,19] Further, as a result of the highly concentrated solution and low boiling point of the solvent, the films crystallize, i.e., turns black, almost immediately after the wet film is coated. To elucidate these fast crystallization dynamics, we applied high-speed synchrotron in situ X-ray diffraction (XRD) to record the structural evolution of the film every 100 ms for 22 s and then every 3 s for 1300 s. At 360 s, the blade stage temperature is increased to 100 °C to monitor the effect of annealing on the film structure (Figure S5 shows the temperature, X-ray scan, and time profiles). The full XRD results are presented in Figure S5. Unlike the MHP films from dimethyl sulfoxide- and dimethylformamide-based solution chemistries,[20,21] no intermediate state is observed during the precursor solution–film crystallization process (Figure S5). In Figure 2b, the peak area of the characteristic $MAPbI_3$ XRD peak, i.e., $MAPbI_3(110)$ at $q \approx 1$ A^{-1}, is tracked. The film reaches more than 60% relative crystallinity (XRD peak area is normalized to the highest peak area) within 1 s of film deposition (Figure 2b, right) and 98% relative crystallinity at room temperature (after ~110 s), confirming formation of $MAPbI_3$ at room temperature.

We further explored the crystal growth orientation dynamics during the film deposition process. Crystallization orientation, grain boundary type (i.e., horizontal, vertical), and grain density have significant impact on the optoelectronic properties of perovskite solar cells (PSCs).[22,23] To elucidate the crystal growth orientation dynamics quantitatively, the Maier–Saupe orientation parameter (m_{MS})[24] is fitted from

$$I_{MS}(\chi) = \frac{\sqrt{\pi}}{2Z\sqrt{m_{MS}}\cos\chi}\exp(m_{MS}\cos^2\chi)\mathrm{erf}(\sqrt{m_{MS}}\cos\chi) \quad (1)$$

where $I_{MS}(\chi)$ is the intensity of the diffraction arch as a function of the angle χ, Z is a normalization constant, and "erf" is the error function. Though originally proposed in the context of liquid crystals, m_{MS} has shown to be a powerful analytical tool to quantify orientation in other material systems as well.[25,26] It allows one to obtain the Maier–Saupe orientational distribution function $f_{MS}(\beta)$ by

$$f_{MS}(\beta) = \frac{1}{Z}\exp(m_{MS}\cos^2\beta) \quad (2)$$

where β is the tilting angle from the film normal. As illustrated in Figure S6, the higher the m_{MS}, the sharper the $f_{MS}(\beta)$ peak value and, thus, more oriented crystals. Fitting results of the in situ XRD data of $MAPbI_3(110)$ show m_{MS} over 50 within the first second of film coating, and it does not significantly change over the course of evaporation at room temperature and 100

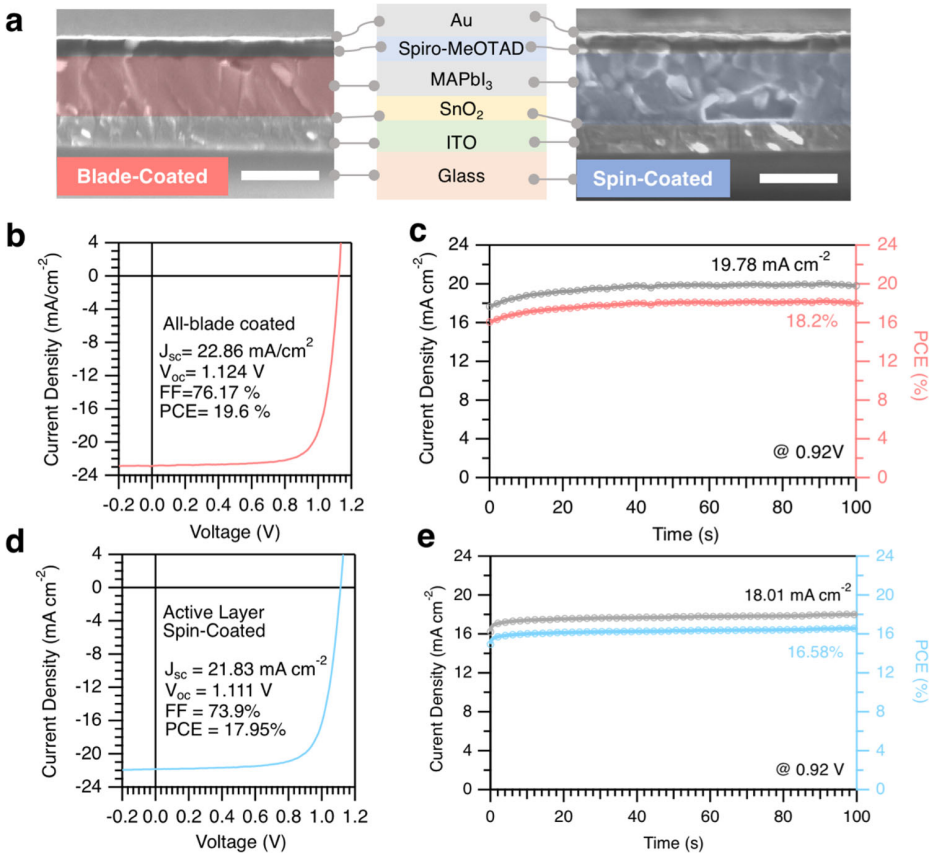

Figure 4. (a) Cross-sectional SEM image of an all-blade-coated PSC (left) and active layer spin-coated (right). The scale bar is 500 nm. (b,c) All-blade-coated champion device characterization: *J*–*V* curve (b) and SPO (c), (d,e) Active layer spin-coated champion device characterization: *J*–*V* curve (d) and SPO (e).

°C, indicating that the film is highly oriented toward (*hk*0),[27] where $h = k$, once coated. Shear force and the resulting balance of Couette flow, Marangoni flow, and capillary flow are likely the driving forces for oriented growth in meniscus-guided coating. To test this, MHP films were spin-coated from the same solution composition. Compared to the optimized spin-coated films,[17] the blade-coated films show strong periodic XRD peaks that correspond to the (*hk*0) of the $MAPbI_3$ (Figure 2c). This is further confirmed by the ex situ 2D XRD patterns of a spin-coated film and a blade-coated film (Figure 2d). The spin-coated film shows a m_{MS} of 3.83 (Figure S7a), whereas the blade-coated film shows m_{MS} reaching 250 (Figure S7b), demonstrating the highly oriented film for this ink formulation results from applying the blade coating process described.

The morphology of the films is examined with scanning electron microscopy (SEM). Top-surface and cross-sectional SEM images for both the blade-coated films and spin-coated films are presented in Figure 3a,b, respectively. Although domain sizes of over 500 nm are observed with spin-coated films (Figure 3a, right), the bulk of the layer appears highly inhomogeneous and with regions of contrast running both vertically and horizontally (Figure 3b, top), consistent with the relatively random orientation of grains observed in the XRD. In blade-coated films, the morphology of the surface as observed by SEM(Figure 3a, left) is less pronounced. Instead, some white spots are observed that are likely due to the excess PbI_2 in the solution.[28] Moreover, again consistent with the orientation as determined from XRD, the films are more homogeneous and compact (Figure 3b, bottom) in blade-coated films due to the balance of linear coating and liquid-film drying (i.e., balance between the Couette flow, Marangoni flow, and capillary flow). The uniformity of the blade-coated film is further investigated with profilometry, where a surface roughness RMS of 3.05 nm is obtained for blade-coated films. This is comparable with the surface roughness from a spin-coated film (RMS = 4.89 nm, Figure 3c). It is worth noting that blade coating is performed in an ambient environment at room temperature and at a blade coating speed of 2.5–3 m min^{-1}, which is much higher than that of previous demonstrations of blade-coated perovskites (0.3–0.5 m min^{-1}).[7,8,29,30]

Blade-Coated Solar Cells. Regular (n–i–p) structure PSCs are constructed with the active layer deposited with blade coating. SnO_2 (blade-coated from aqueous SnO_2 nanoparticles) and spiro-MeOTAD (blade-coated from spiro-MeOTAD in chlorobenzene) are used as electron and hole transport layers, respectively. ITO on glass and Au is used as the bottom and top contacts, respectively. A cross-sectional SEM image of the all-blade-coated device is presented in Figure 4a (left). For comparison, the cross-sectional SEM of a spin-coated device is shown in Figure 4a (right). Consistent with earlier observation, the coating enables films with minimal horizontal grain boundaries. Current density–voltage (*J*–*V*) curves for spin- and blade-coated devices are presented in Figure 4b,d, respectively. The champion blade-coated device

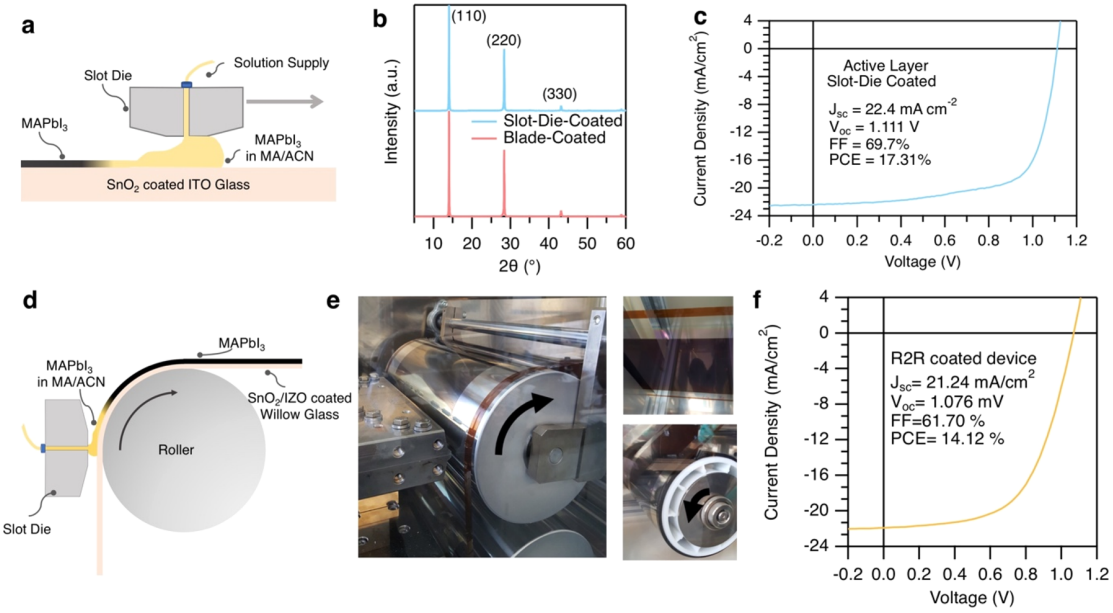

Figure 5. (a–c) Schematic representation of slot-die coating on rigid glass (a), film XRD (b), and device performance (c). (d) Schematic representation of slot-die coating on flexible glass with a R2R coater. (e) Photograph of R2R coating in action (left), after annealing (top right), and the rewinding process (bottom right). (f) *J–V* curve of the champion R2R-coated device.

shows a reverse-scanned (where the voltage is scanned from open-circuit to short-circuit) PCE of 19.6%, with a short-circuit current (J_{SC}) of 22.86 mA cm^{-2}, open-circuit voltage (V_{OC}) of 1.124 V, and fill factor (FF) of 76.17% (Figure S8 for statistics). We compared this with spin-coated devices from the same solvent system with optimized concentration and processing and obtained a champion device of PCE = 17.96%, J_{SC} = 21.83 mA cm^{-2}, V_{OC} = 1.111 V, and FF = 73.9% (Figure S8 for statistics), which is consistent with other reported spin-coated devices with the same solution and processing.[17] Typically, transfer of spin coating to blade coating leads to reduce device performance,[6] here we invert this behavior with the demonstration of superior blade-coated devices. The high V_{OC} with a blade-coated device is especially impressive as it directly reflects the minimized nonradiative losses of the solar cell, indicating the high quality of blade-coated films. It is interesting that, despite thicker MHP films (~280 nm for blade-coated films, ~320 nm with spin-coated films), the spin-coated devices show lower J_{SC}, which suggests poor charge transport in the spin-coated films. This is further confirmed with external quantum efficiency (EQE) measurements (Figure S9a,b) where the integrated J_{SC} from the blade-coated device yields 21.75 mA cm^{-2}, whereas the spin-coated device shows 17.5 mA cm^{-2}.

While high reverse-scanned efficiencies are obtained with the n–i–p structure, all-blade-coated cells, the forward scans (voltage scanned from the short-circuit to open-circuit voltage) (Figure S10) and the stabilized power out (SPO) of the devices (Figure 4c,e) are lower than those of the reverse scans. Such differences are reported to be less pronounced in p–i–n structured devices.[12] To test if the developed blade-coating processing of $MAPbI_3$ is compatible with the p–i–n structure to reduce the efficiency gap of reverse scanned PCE and SPO, the device structure was completely redesigned to an inverted (p–i–n) structure: ITO/PEDOT:PSS/blade-coated perovskite/C60/BCP/Ag (Figure S11). The resulting device *J–V* scans (both forward and reverse) and SPO show no difference: 10.83% reverse PCE, 10.73% forward PCE, and 10.45% SPO. Although there is significant room for improving these devices with p–i–n structure, the elimination of hysteresis in this structure strongly supports that the efficiency difference (reverse PCE to forward PCE and SPO) displayed with blade-coated devices could be effectively reduced with better design of the charge transport layers.

Slot-Die and R2R Coating. Blade coating is simple and effective for making high-performance PSCs, but controlled blade coating on R2R is challenging. Slot-die coating, on the other hand, is perfectly implementable with R2R coating.[31−33] Slot-die coating is also a meniscus-guided laminar flow coating, and it fundamentally shares most flow dynamics with blade coating (Figure 5a). Therefore, the blade-coating approach already employed can be transferred to slot-die coating.[18] As shown in Figure 5a, $MAPbI_3$ films were coated on the SnO_2/ITO/glass substrate with slot-die coating using the exact same solution. The resulting films were examined with XRD to ensure that there is no process-induced structural change. Similar to the blade-coated films, the XRD pattern exhibits highly oriented $MAPbI_3$ where the XRD peaks that correspond to the (*hk*0) are significantly more intense than other peaks (Figure 5b). The observed surface morphology in the slot-die-coated film is more structured compared to the blade-coated film (Figure S12), which is likely due to variations in flow rate and resulting nucleation rate. Nevertheless, resulting devices show efficiency of 17.31% with J_{SC} of 22.4 mA cm^{-2}, V_{OC} of 1.111 V, and FF of 69.5% (Figure 5c). SPO and device statistics are shown in Figures S13 and S14, respectively. Compared to the 19.6% PCE from blade coating, the largest loss is in the FF, which is likely due to inhomogeneity at the surfaces and within the film, which results in resistive loss with slot-die coating (Figure S12). We believe that such loss can be improved with further optimization of the coating parameters.

We tested our slot-die coating method on the R2R printing of perovskite on a 20 m long, 100 μm thick flexible Corning Willow Glass substrate. Indium zinc oxide (IZO) is R2R

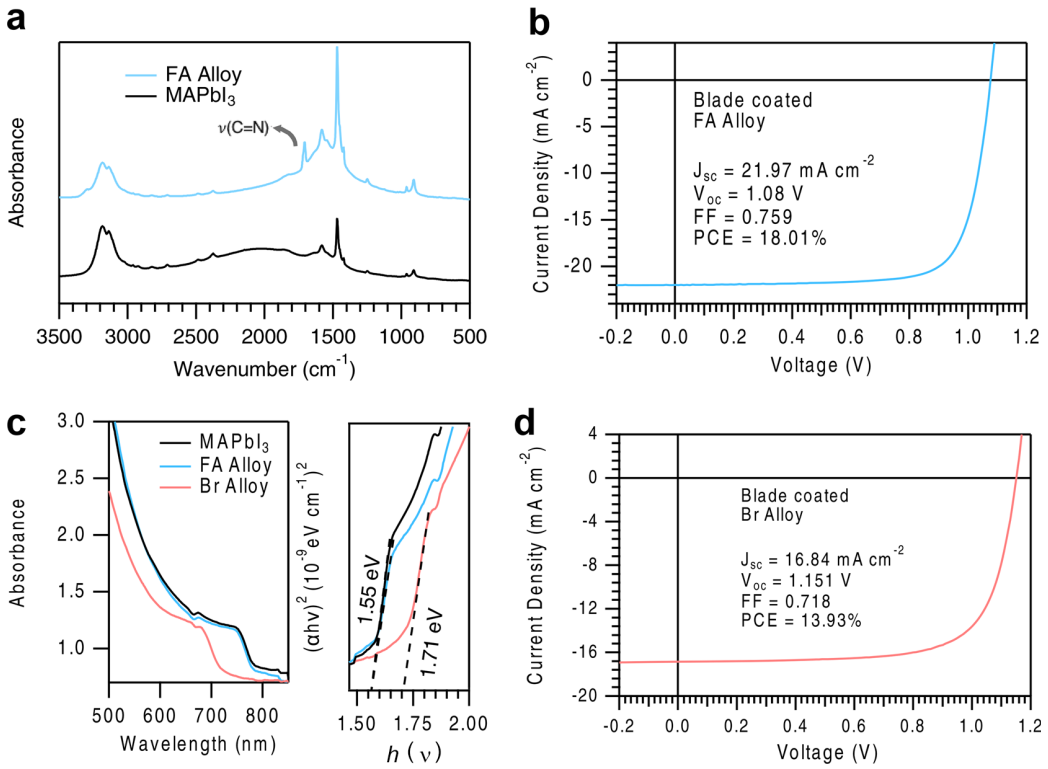

Figure 6. (a) FTIR spectrum of the solution stoichiometry of the $FA_{0.125}MA_{0.875}PbI_3$-based film and $MAPbI_3$. (b) *J–V* curve of the FA alloyed PSC. (c) Absorption spectra (left) and Tauc plot (right) of the solution stoichiometry of the $FA_{0.125}MA_{0.875}Pb(I_{0.67}Br_{0.33})_3$ based film showing a bandgap of 1.71 eV after Br incorporation. (d) *J–V* curve of the solution stoichiometry of the $FA_{0.125}MA_{0.875}Pb(I_{0.67}Br_{0.33})_3$-based device.

sputtered on the Willow Glass, as reported elsewhere,[34] and general properties of flexible glass and device fabrication techniques utilizing it have likewise been reported.[35,36] It was shown previously that flexible PSCs with IZO as the transparent conductive oxide have achieved over 18% PCE.[37] After R2R IZO coating, SnO_2 is slot-die R2R-coated from $Sn(OCH(CH_3)_2)_4$ in isopropanol (IPA) solution.[38] The $Sn(OCH(CH_3)_2)_4$ in IPA solution was chosen over the SnO_2 nanoparticle in water solution to avoid room-temperature wettability problems with water-based solutions. The perovskite layer was then slot-die-coated on the SnO_2, as shown in Figure 5d. A picture of R2R printing in action is presented in Figure 5e, where the film coating (Figure 5e left), after annealing (Figure 5e, top right), and rewinding process (Figure 5e, bottom right) are illustrated. Two videos showing the coating process are provided in the Supporting Information. The resulting R2R-coated perovskite film is then cut into square-inch pieces, spiro-MeOTAD is spin-coated, and evaporation of Au electrodes finishes the devices. The resulting R2R devices (device area: 0.15 cm^2) show an efficiency of 14.12% with J_{SC} of 21.24 mA cm^{-2}, V_{OC} of 1.076 V, and FF of 61.7% (Figure 5f). Device statistics can be found in Figure S15. This efficiency is significant, as it is not only among the highest-efficiencies for R2R-coated thin film solar cells, but was also processed at room temperature in an ambient environment. Details of all R2R slot-die coating parameters are presented in the Materials and Methods section, but one parameter of interest is the amount of the MHP solution applied for R2R coating: ~3 mL m^{-2}. To put this number into perspective, 21.42 L of ink will be sufficient to coat a standard soccer field size area (7140 m^2). With a 15% MHP module PCE,[1] 21.42 L of ink can produce 1.071 MW of power. Combining this with the high throughput and low production line labor cost of R2R, we believe that this will make PSCs the cheapest PV materials after addressing the cost of the hole transport material and top contact. Furthermore, with such small usage of the solution, the potential negative environmental impacts of R2R perovskite processing will be at a minimal level.

Beyond $MAPbI_3$. Having demonstrated high-efficiency $MAPbI_3$ PSCs, it is of interest to investigate the applicability of the R2R perovskite printing method to other perovskite materials systems that contain formamidinium (FA) or bromide (Br) because engineering perovskite compositions allows for higher efficiency,[39] better stability (both thermally and compositionally),[40] and bandgap tuning.[41] We first blade-coated films from a solution that has the stoichiometry of $FA_{0.125}MA_{0.875}PbI_3$. To confirm the incorporation of FA, FTIR measurements were performed and are presented in Figure 6a. The presence of FA in the perovskite film is confirmed with the prominent resonance of the C═N symmetric stretching at 1712 cm^{-1}.[42] Devices with 18.01% PCE, a J_{SC} of 21.97 mA cm^{-2}, V_{OC} = 1.08 V, and FF = 75.9% are obtained with the FA alloy (Figure 6b). Statistics are presented in Figure S16. Further increasing the FA content in the solution, however, resulted in decreased PV performance, as shown in Figure S16. This observation is currently under investigation. The printing method was further tested with an X-site alloy. A precursor solution with solution stoichiometry of $FA_{0.125}MA_{0.875}Pb(I_{0.67}Br_{0.33})_3$ was prepared and blade-coated (Supporting Information). The incorporation of Br in the final film was confirmed by an absorption blue shift due to the increased

bandgap of 1.71 eV (Figure 6c). With this active layer, devices with 13.93% PCE, a J_{SC} of 16.84 mA cm^{-2}, a V_{OC} of 1.15 V, and a FF of 71.8% were obtained (Figure 6d). Statistics are shown in Figure S17. EQE measurement (Figure S18) also confirms the increased bandgap, with blue-shifted EQE spectra. This demonstration of high efficiency with high bandgap brings us one step closer to reality to create all-R2R-printed, low-cost, high-efficiency perovskite–perovskite tandems.[43]

In summary, we demonstrated a method to form crystalline, uniaxially oriented, smooth perovskite films from R2R printing techniques. Owing to the low boiling point of the solvent, the R2R coating was performed at room temperature in ambient environment. With mechanistic understanding from high-speed in situ XRD measurements, PSCs with PCEs of 19.6, 17.3, and 14.1% were produced with blade coating, slot-die coating, and partial R2R slot-die coating, respectively. The printing method is demonstrated not to be limited to the prototype perovskite materials (i.e., $MAPbI_3$); we show it is compatible with other perovskite compositions such as high-bandgap (1.71 eV) FA and Br alloys, showing the potential of R2R slot-die-coated, high-throughput, low-cost, high-efficiency perovskite–perovskite tandems as a possible way to address the world's terawatt energy challenge.[1,44]

AUTHOR INFORMATION

Corresponding Author

*E-mail: maikel.van.hest@nrel.gov.

ORCID

Benjia Dou: 0000-0001-6038-5561

Lance M. Wheeler: 0000-0002-1685-8242

Kai Zhu: 0000-0003-0908-3909

Author Contributions

B.D. and M.F.A.M.v.H. conceived and designed the project. B.D. prepared and characterized all of the films and devices. J.B.W. assisted on slot-die-coated devices and R2R slot-die-coated devices. K.B. performed the in situ XRD measurements, and C.J.T. supervised. D.T.M. prepared the solvent. L.M.W. performed the FTIR measurements. J.R. and N.J.B. assisted on charge transport layer coating. S.M.G. prepared the flexible Willow Glass substrates and contributed R2R coating. J.J.B. performed 2D-XRD measurements. F.S.B. and S.E.S. contributed to the discussion and advised B.D. M.F.A.M.v.H. supervised the entire project. B.D. wrote the first draft of the paper. All of the authors discussed the results and contributed to the writing of the paper.

Notes

The authors declare no competing financial interest.

ACKNOWLEDGMENTS

This article was partially based upon work supported under the U.S.–India Partnership to Advance Clean Energy Research (PACE-R) for the Solar Energy Research Institute for India and the United States (SERIIUS), funded jointly by the U.S. Department of Energy (Office of Science, Office of Basic Energy Sciences, and Energy Efficiency and Renewable Energy, Solar Energy Technology Program, under Subcontract DE-AC36- 08GO28308 to the National Renewable Energy Laboratory (NREL), Golden, Colorado) and the Government of India, through the Department of Science and Technology under Subcontract IUSSTF/JCERDC- SERIIUS/2012 dated Nov 22, 2012. The article was partially supported by the Hybrid Perovskite Solar Cell (HPSC) Program funded the Solar Energy Technology Office (SETO) under Contract No. DE-AC36-08-GO28308 at NREL. B.D., D.T.M., J.J.B., K.Z., and M.F.A.M.v.H. were supported by the HPSC Program funded by SETO under DOE Contract No. DE-AC36-08-GO28308 with NREL. J.B.W. and L.M.W acknowledge support from the Laboratory Directed Research and Development (LDRD) program and NREL. The work at the Stanford Synchrotron Radiation Lightsource was funded by the Department of Energy under Contract No. DE-AC02-76SF00515. The Stanford Synchrotron Radiation Lightsource at the SLAC National Accelerator Laboratory is a national user facility operated by Stanford University on behalf of the U.S. Department of Energy, Office of Basic Energy Sciences. Part of this work was performed at the Stanford Nano Shared Facilities (SNSF), supported by the National Science Foundation under Award ECCS-1542152. We thank the Center for Advanced Microelectronic Manufacturing (CAMM) at Binghamton University for coating IZO on Willow Glass. J.R. and N.J.B. acknowledge the Science Undergraduate Laboratory Internship (SULI) program at NREL.

REFERENCES

(1) Berry, J. J.; Van De Lagemaat, J.; Al-Jassim, M. M.; Kurtz, S.; Yan, Y.; Zhu, K. Perovskite Photovoltaics: The Path to a Printable Terawatt-Scale Technology. *ACS Energy Lett.* **2017**, *2* (11), 2540–2544.

(2) National Renewable Energy Laboratory. *Best Research-Cell Efficiencies*. https://www.nrel.gov/pv/assets/pdfs/pv-efficiencies-07-17-2018.pdf (accessed May 5, 2018).

(3) Bruening, K.; Dou, B.; Simonaitis, J.; Lin, Y.-Y.; van Hest, M. F. A. M.; Tassone, C. J. Scalable Fabrication of Perovskite Solar Cells to Meet Climate Targets. *Joule* **2018**, DOI: 10.1016/j.joule.2018.09.014.

(4) Steirer, K. X.; Schulz, P.; Teeter, G.; Stevanovic, V.; Yang, M.; Zhu, K.; Berry, J. J. Defect Tolerance in Methylammonium Lead Triiodide Perovskite. *ACS Energy Lett.* **2016**, *1* (2), 360–366.

(5) Krebs, F. C. Fabrication and Processing of Polymer Solar Cells: A Review of Printing and Coating Techniques. *Sol. Energy Mater. Sol. Cells* **2009**, *93* (4), 394–412.

(6) Li, Z.; Klein, T. R.; Kim, D. H.; Yang, M.; Berry, J. J.; van Hest, M. F. A. M.; Zhu, K. Scalable Fabrication of Perovskite Solar Cells. *Nat. Rev. Mater.* **2018**, *3* (4), 18017.

(7) Yang, M.; Li, Z.; Reese, M. O.; Reid, O. G.; Kim, D. H.; Siol, S.; Klein, T. R.; Yan, Y.; Berry, J. J.; van Hest, M. F. A. M.; et al. Perovskite Ink with Wide Processing Window for Scalable High-Efficiency Solar Cells. *Nat. Energy* **2017**, *2* (5), 17038.

(8) Tang, S.; Deng, Y.; Zheng, X.; Bai, Y.; Fang, Y.; Dong, Q.; Wei, H.; Huang, J. Composition Engineering in Doctor-Blading of Perovskite Solar Cells. *Adv. Energy Mater.* **2017**, *7* (18), 1700302.

(9) Deng, Y.; Zheng, X.; Bai, Y.; Wang, Q.; Zhao, J.; Huang, J. Surfactant-Controlled Ink Drying Enables High-Speed Deposition of

Perovskite Films for Efficient Photovoltaic Modules. *Nat. Energy* **2018**, *3*, 560−566.
(10) He, M.; Li, B.; Cui, X.; Jiang, B.; He, Y.; Chen, Y.; O'Neil, D.; Szymanski, P.; Ei-Sayed, M. A.; Huang, J.; et al. Meniscus-Assisted Solution Printing of Large-Grained Perovskite Films for High-Efficiency Solar Cells. *Nat. Commun.* **2017**, *8* (May), 16045.
(11) Wu, W.; Wang, Q.; Fang, Y.; Shao, Y.; Tang, S.; Deng, Y.; Lu, H.; Liu, Y.; Li, T.; Yang, Z.; et al. Molecular Doping Enabled Scalable Blading of Efficient Hole-Transport-Layer-Free Perovskite Solar Cells. *Nat. Commun.* **2018**, *9* (1), 1625.
(12) Seok, S. Il; Grätzel, M.; Park, N.-G. Methodologies toward Highly Efficient Perovskite Solar Cells. *Small* **2018**, *14*, 1704177.
(13) Jeon, N. J.; Noh, J. H.; Kim, Y. C.; Yang, W. S.; Ryu, S.; Seok, S. Il. Solvent Engineering for High-Performance Inorganic−Organic Hybrid Perovskite Solar Cells. *Nat. Mater.* **2014**, *13* (9), 897−903.
(14) Li, X.; Bi, D.; Yi, C.; Decoppet, J.-D.; Luo, J.; Zakeeruddin, S. M.; Hagfeldt, A.; Gratzel, M. A Vacuum Flash-Assisted Solution Process for High-Efficiency Large-Area Perovskite Solar Cells. *Science (Washington, DC, U. S.)* **2016**, *353* (6294), 58−62.
(15) Sanchez, S.; Hua, X.; Phung, N.; Steiner, U.; Abate, A. Flash Infrared Annealing for Antisolvent-Free Highly Efficient Perovskite Solar Cells. *Adv. Energy Mater.* **2018**, 1702915.
(16) Huang, F.; Dkhissi, Y.; Huang, W.; Xiao, M.; Benesperi, I.; Rubanov, S.; Zhu, Y.; Lin, X.; Jiang, L.; Zhou, Y.; et al. Gas-Assisted Preparation of Lead Iodide Perovskite Films Consisting of a Monolayer of Single Crystalline Grains for High Efficiency Planar Solar Cells. *Nano Energy* **2014**, *10*, 10−18.
(17) Noel, N. K.; Habisreutinger, S. N.; Wenger, B.; Klug, M. T.; Hörantner, M. T.; Johnston, M. B.; Nicholas, R. J.; Moore, D. T.; Snaith, H. J. A Low Viscosity, Low Boiling Point, Clean Solvent System for the Rapid Crystallisation of Highly Specular Perovskite Films. *Energy Environ. Sci.* **2017**, *10* (1), 145−152.
(18) Gu, X.; Shaw, L.; Gu, K.; Toney, M. F.; Bao, Z. The Meniscus-Guided Deposition of Semiconducting Polymers. *Nat. Commun.* **2018**, *9* (1), 534.
(19) Qu, G.; Kwok, J. J.; Diao, Y. Flow-Directed Crystallization for Printed Electronics. *Acc. Chem. Res.* **2016**, *49* (12), 2756−2764.
(20) Nenon, D. P.; Christians, J. A.; Wheeler, L. M.; Blackburn, J. L.; Sanehira, E. M.; Dou, B.; Olsen, M. L.; Zhu, K.; Berry, J. J.; Luther, J. M. Structural and Chemical Evolution of Methylammonium Lead Halide Perovskites during Thermal Processing from Solution. *Energy Environ. Sci.* **2016**, *9* (6), 2072−2082.
(21) Dou, B.; Pool, V. L.; Toney, M. F.; Van Hest, M. F. A. M. A. M. Radiative Thermal Annealing/in Situ X-Ray Diffraction Study of Methylammonium Lead Triiodide: Effect of Antisolvent, Humidity, Annealing Temperature Profile, and Film Substrates. *Chem. Mater.* **2017**, *29* (14), 5931−5941.
(22) Kim, D. H.; Park, J. J.-S. S.; Li, Z.; Yang, M.; Park, J. J.-S. S.; Park, I. J.; Kim, J. Y.; Berry, J. J.; Rumbles, G.; Zhu, K. 300% Enhancement of Carrier Mobility in Uniaxial-Oriented Perovskite Films Formed by Topotactic-Oriented Attachment. *Adv. Mater.* **2017**, *29* (23), 1606831.
(23) Ji, F.; Pang, S.; Zhang, L.; Zong, Y.; Cui, G.; Padture, N. P.; Zhou, Y. Simultaneous Evolution of Uniaxially Oriented Grains and Ultralow-Density Grain-Boundary Network in $CH_3NH_3PbI_3$Perovskite Thin Films Mediated by Precursor Phase Metastability. *ACS Energy Lett.* **2017**, *2* (12), 2727−2733.
(24) Deutsch, M. Orientational Order Determination in Liquid Crystals by X-Ray Diffraction. *Phys. Rev. A: At., Mol., Opt. Phys.* **1991**, *44* (12), 8264−8270.
(25) Davidson, P. X-Ray Diffraction by Liquid Crystalline Side-Chain Polymers. *Prog. Polym. Sci.* **1996**, *21* (5), 893−950.
(26) Ahir, S. V.; Squires, A. M.; Tajbakhsh, A. R.; Terentjev, E. M. Infrared Actuation in Aligned Polymer-Nanotube Composites. *Phys. Rev. B: Condens. Matter Mater. Phys.* **2006**, *73* (8), 1−12.
(27) Krishnamurthy, V. V.; Mankey, G. J.; He, B.; Piao, M.; Wiest, J. M.; Nikles, D. E.; Porcar, L.; Robertson, J. L. Orientational Distributions and Nematic Order of Rodlike Magnetic Nanoparticles in Dispersions. *Phys. Rev. E - Stat. Nonlinear, Soft Matter Phys.* **2008**, *77* (3), 1−8.
(28) Pool, V. L.; Dou, B.; Van Campen, D. G.; Klein-Stockert, T. R.; Barnes, F. S.; Shaheen, S. E.; Ahmad, M. I.; van Hest, M. F. A. M.; Toney, M. F. Thermal Engineering of FAPbI3 Perovskite Material via Radiative Thermal Annealing and in Situ XRD. *Nat. Commun.* **2017**, *8*, 14075.
(29) Deng, Y.; Wang, Q.; Yuan, Y.; Huang, J. Vivid Colorful Hybrid Perovskite Solar Cells by Doctor-Blade Coating with Perovskite Photonic Nanostructures. *Mater. Horiz.* **2015**, *2* (6), 578−583.
(30) Zhong, Y.; Munir, R.; Li, J.; Tang, M.-C.; Niazi, M. R.; Zhao, K.; Amassian, A.; et al. Blade-Coated Organolead Triiodide Perovskite Solar Cells with Efficiency > 17%: An In Situ Investigation. *ACS Energy Lett.* **2018**, *3*, 1078.
(31) Hwang, K.; Jung, Y. S.; Heo, Y. J.; Scholes, F. H.; Watkins, S. E.; Subbiah, J.; Jones, D. J.; Kim, D. Y.; Vak, D. Toward Large Scale Roll-to-Roll Production of Fully Printed Perovskite Solar Cells. *Adv. Mater.* **2015**, *27* (7), 1241−1247.
(32) Heo, Y. J.; Kim, J. E.; Weerasinghe, H.; Angmo, D.; Qin, T.; Sears, K.; Hwang, K.; Jung, Y. S.; Subbiah, J.; Jones, D. J.; et al. Printing-Friendly Sequential Deposition via Intra-Additive Approach for Roll-to-Roll Process of Perovskite Solar Cells. *Nano Energy* **2017**, *41*, 443−451.
(33) Kim, J. E.; Jung, Y. S.; Heo, Y. J.; Hwang, K.; Qin, T.; Kim, D. Y.; Vak, D. Slot Die Coated Planar Perovskite Solar Cells via Blowing and Heating Assisted One Step Deposition. *Sol. Energy Mater. Sol. Cells* **2018**, *179*, 80−86.
(34) Switzer, J. C., III; Poliks, M. D. Roll-to-Roll Processing of Flexible Glass. In *Flexible Glass: Enabling Thin, Lightweight, and Flexible Electronics*; Garner, S. M., Ed.; Wiley-Scrivener: Hoboken, NJ, 2017; pp 85−128.
(35) Garner, S.; Glaesemann, S.; Li, X. Ultra-Slim Flexible Glass for Roll-to-Roll Electronic Device Fabrication. *Appl. Phys. A: Mater. Sci. Process.* **2014**, *116* (2), 403−407.
(36) Garner, S. M. *Flexible Glass : Enabling Thin, Lightweight, and Flexible Electronics*; Wiley-Scrivener: Hoboken, NJ, 2017.
(37) Dou, B.; Miller, E. M.; Christians, J. A.; Sanehira, E. M.; Klein, T. R.; Barnes, F. S.; Shaheen, S. E.; Garner, S. M.; Ghosh, S.; Mallick, A.; et al. High-Performance Flexible Perovskite Solar Cells on Ultrathin Glass: Implications of the TCO. *J. Phys. Chem. Lett.* **2017**, *8* (19), 4960−4966.
(38) Jung, K.-H.; Seo, J.-Y.; Lee, S.; Shin, H.; Park, N.-G. Solution-Processed SnO2 Thin Film for Hysteresis-Less 19.2% Planar Perovskite Solar Cell. *J. Mater. Chem. A* **2017**, *5*, 24790−24803.
(39) Jeon, N. J.; Noh, J. H.; Yang, W. S.; Kim, Y. C.; Ryu, S.; Seo, J.; Seok, S. Il. Compositional Engineering of Perovskite Materials for High-Performance Solar Cells. *Nature* **2015**, *517* (7535), 476−480.
(40) Correa-Baena, J. P.; Saliba, M.; Buonassisi, T.; Gratzel, M.; Abate, A.; Tress, W.; Hagfeldt, A. Promises and Challenges of Perovskite Solar Cells. *Science (Washington, DC, U. S.)* **2017**, *358* (6364), 739−744.
(41) Knutson, J. L.; Martin, J. D.; Mitzi, D. B. Tuning the Band Gap in Hybrid Tin Iodide Perovskite Semiconductors Using Structural Templating. *Inorg. Chem.* **2005**, *44* (13), 4699−4705.
(42) Dou, B.; Wheeler, L. M.; Christians, J. A.; Moore, D. T.; Harvey, S.; Berry, J. J.; Barnes, F. S.; Shaheen, S. E.; van Hest, M. F. A. M. Degradation of Highly Alloyed Metal Halide Perovskite Precursor Inks: Mechanism and Storage Solutions. *ACS Energy Lett.* **2018**, *3* (4), 979−985.
(43) Eperon, G. E.; Leijtens, T.; Bush, K. A.; Prasanna, R.; Green, T.; Wang, J. T.-W.; McMeekin, D. P.; Volonakis, G.; Milot, R. L.; May, R.; et al. Perovskite-Perovskite Tandem Photovoltaics with Optimized Band Gaps. *Science (Washington, DC, U. S.)* **2016**, *354* (6314), 861−865.
(44) Haegel, N. M.; Margolis, R.; Buonassisi, T.; Feldman, D.; Froitzheim, A.; Garabedian, R.; Green, M.; Glunz, S.; Henning, H.-M. M.; Holder, B.; et al. Terawatt-Scale Photovoltaics: Trajectories and Challenges. *Science (Washington, DC, U. S.)* **2017**, *356* (6334), 141−143.